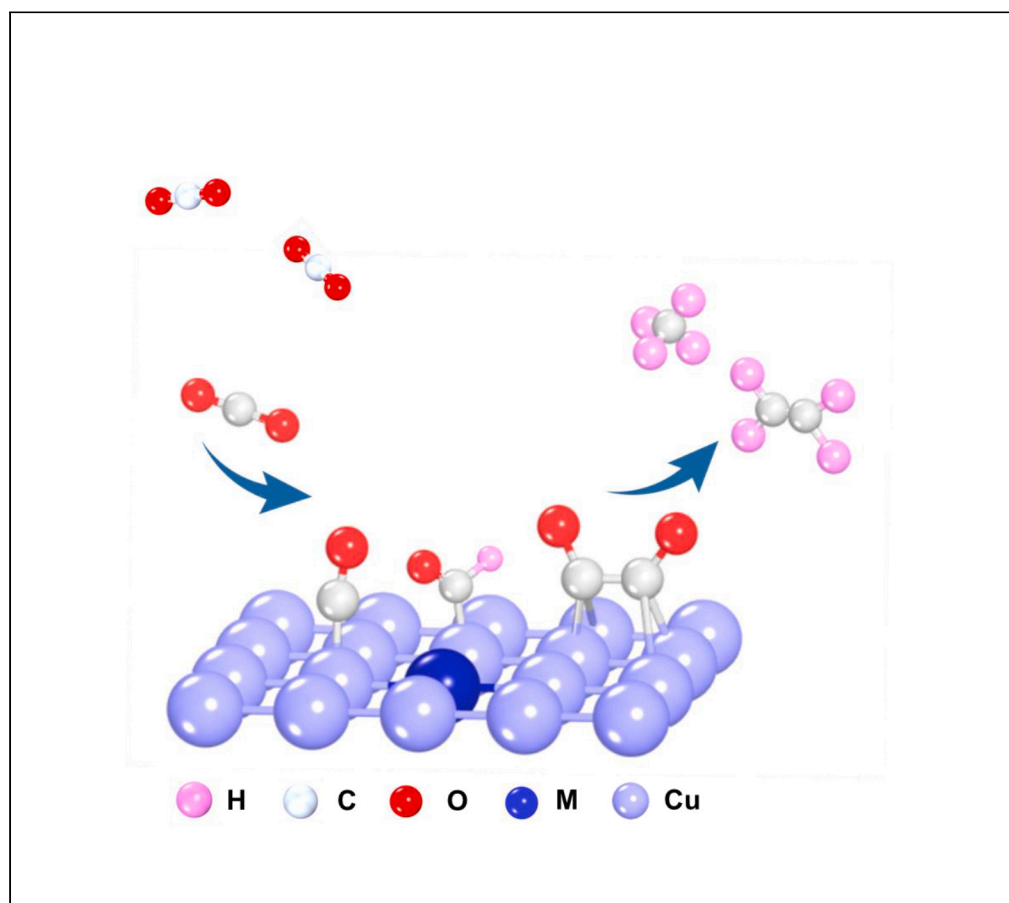


Article

Insights into the mechanism in electrochemical CO₂ reduction over single-atom copper alloy catalysts: A DFT study

Tianfu Liu, Guohui Song, Xiaojun Liu, ..., Qi Wang, Zhangquan Peng, Guoxiong Wang

ltianfu@dicp.ac.cn (T.L.)
wanggx@dicp.ac.cn (G.W.)

Highlights

Electrochemical CO₂ reduction reaction on copper single-atom alloy is studied by DFT

The adsorption mode on copper single-atom alloy catalysts is revealed

The *CO adsorption energy and scaling relations are key to understand the activity

The high coverage of *CO leads to improved activity of C₂ products

Liu et al., iScience 26, 107953
October 20, 2023 © 2023 The Author(s).
<https://doi.org/10.1016/j.isci.2023.107953>

Article

Insights into the mechanism in electrochemical CO₂ reduction over single-atom copper alloy catalysts: A DFT study

Tianfu Liu,^{1,2,6,*} Guohui Song,^{1,3,6} Xiaojun Liu,⁴ Zhou Chen,⁵ Yu Shen,³ Qi Wang,³ Zhangquan Peng,¹ and Guoxiong Wang^{1,7,*}

SUMMARY

Copper single-atom alloy catalysts (M@Cu SAAs) have shown great promise for electrochemical CO₂ reduction reaction (CO₂RR). However, a clear understanding of the CO₂RR process on M@Cu SAAs is still lacking. This study uses density functional theoretical (DFT) calculations to obtain a comprehensive mechanism and the origin of activity of M@Cu SAAs. The importance of the adsorption mode of M@Cu is revealed: key intermediates either adsorbed in the adjacent hollow site around Cu atoms (AD mode) or adsorbed directly on the top site of M (SE mode). AD mode generally exhibits finely tuned binding strengths of key intermediates, which significantly enhances the activity of the catalysts. Increasing the coverage of *CO on the M@Cu with SE mode leads to relocation of the active site, resulting in improved activity of C₂ products. The insights gained in this work have significant implications for rational design strategy toward efficient CO₂RR electrocatalysts.

INTRODUCTION

Electrochemical CO₂ reduction reaction (CO₂RR) powered by renewable electricity has demonstrated an alluring prospect for carbon neutralization and energy storage.¹ Considering CO₂RR process is kinetically and thermodynamically unfavorable due to inertness of CO₂ molecule, developing efficient electrocatalysts is the major challenge for CO₂RR.^{2–4} Copper catalysts have been extensively studied for the excellent activity to convert CO₂ toward energy-dense C₂₊ hydrocarbons and oxygenates.^{5–10} Alloying provides a method to tune copper catalysts' electronic structure, therefore tailors the performances of copper catalysts.^{11–13} However, the mechanism and precise role of secondary elements on Cu alloy catalysts for CO₂RR remains uncertain. Previous studies have suggested that the active sites are the copper atoms adjacent to secondary elements in Pb-Cu, Au-Cu, and Al-Cu alloys.^{5,14,15} These investigations often assume that the primary function of the secondary elements is to modulate the electronic structure of the neighboring copper sites.^{14–16} However, in the case of Pt-Cu, Zn-Cu, and Sn-Cu alloys, it is suggested that secondary elements are active sites themselves.^{17–19} Without a unified picture for the function of secondary element, the underlying mechanism is still unclear in existing literatures.^{20–22} Considering the distinct electronic structures of these secondary elements, it is expected that reaction processes on these copper alloys are significantly dependent on the secondary element.²³ The effect of secondary elements in M@Cu catalysts in regulating the reaction are urgent to be thoroughly investigated.^{24,25}

A recently introduced concept for alloying is the single-atom alloys (SAAs). SAAs are generally consisted of dispersed secondary components (M) dispersed on the surface of the main metal, with no bonding between neighboring secondary elements.²⁶ Due to the weak wavefunction mixing between the minority and majority elements, the SAAs exhibit electronic structures that resemble those of free atoms. This unique characteristic allows SAAs to bypass the linear relations that typically impose limitations in traditional metallic systems.^{27,28} We also notice that the model of copper surface doped with single secondary atoms are extensively used to represent the copper alloy catalysts for theoretical calculations. This suggests that computational results obtained from SAAs models could provide insights into the behavior of general copper alloy catalysts.^{5,14–16}

In this study, we conducted a comprehensive investigation of CO₂RR on M@Cu models using two extensively studied copper surfaces, namely (111) and (100). Our objective was to establish a comprehensive understanding of the CO₂RR on copper alloy catalysts. Through density functional theoretical (DFT) calculations, we systematically simulated over 400 atomic configurations, allowing us to construct detailed energetic profiles for CO₂RR on SAAs. The influence of intrinsic electronic structures of M on the adsorption behavior in M@Cu systems is

¹Dalian Institute of Chemical Physics, Chinese Academy of Sciences, Dalian, Liaoning 116023, China

²University of Chinese Academy of Sciences, Beijing 100039, China

³Dalian Jiaotong University, Dalian 116028, China

⁴School of Chemistry and Chemical Engineering, YuLin University, YuLin, Shanxi 71900, China

⁵College of Materials, Xiamen University, Xiamen, Fujian 361005, China

⁶These authors contribute equally

⁷Lead contact

*Correspondence: ltianfu@dicp.ac.cn (T.L.), wanggx@dicp.ac.cn (G.W.)

<https://doi.org/10.1016/j.isci.2023.107953>



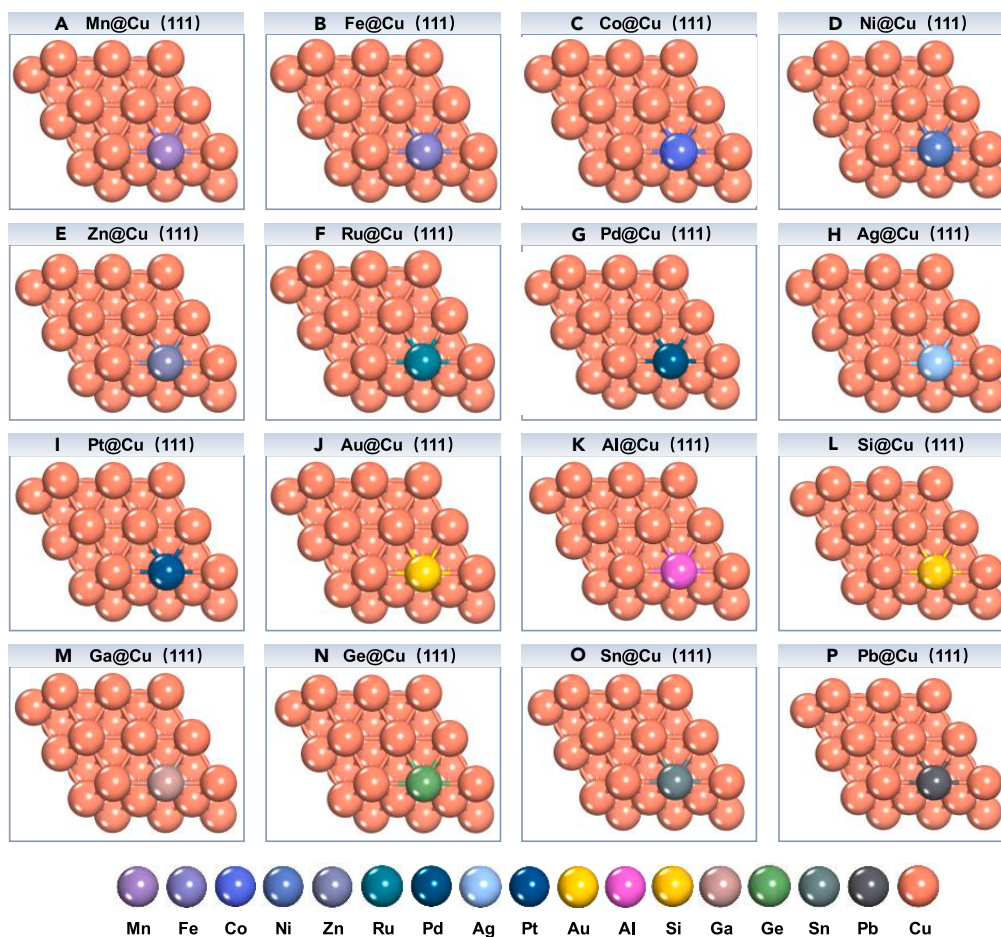


Figure 1. The M@Cu(111) models for DFT calculations

(A–P) Various M@Cu(111) models with one of the surface Cu atom substituted with secondary M atom.

elucidated. Specifically, we found that M@Cu systems with p-block or d-block elements possessing a full d-shell tend to adsorb key intermediates on the hollow sites around Cu atoms adjacent to M. On the other hand, M@Cu systems with open d-shelled M directly adsorb the intermediates on the top site of M. The different adsorption behavior highlights the importance of the intrinsic electronic structure of M in determining reaction mechanisms on M@Cu catalysts. A favorable deviation from the scaling relations of intermediate binding results in a decreased energy barrier toward C₁ and C₂ product. We also observed that increasing the *CO coverage on the catalyst surface changes the favorable active sites for CO₂RR, which plays a crucial role in enhancing the C-C coupling reaction on M@Cu catalysts, thereby promoting the C₂ products. These findings underscore the significance of understanding and manipulating the electronic structure, adsorption of key intermediates, and scaling relations for effective performance in CO₂RR.

RESULTS AND DISCUSSION

Stability of M@Cu

Cu(111) and Cu(100) are the two primary basal facets of copper catalysts that have been extensively studied, because Cu(111) provides a model for a stepped site, and Cu(100) represents a flat surface for catalytic reaction.^{29–31} As shown in Figures 1A–1P, we built M@Cu(111) and M@Cu(100) models by substituting one Cu atom on the surface with one M atom. The stability of M@Cu SAAs is evaluated using binding energy and dissolution potential, which are important factors in determining the fabrication and stability of SAAs. The binding energy represents the strength of the interaction between the M atom and the Cu surface. A higher binding energy indicates a more stable adsorption configuration, suggesting that the M atom is firmly anchored on the Cu surface. The dissolution potential indicates stability of the M@Cu SAA under reaction conditions. A higher dissolution potential indicates greater resistance to dissolution, suggesting enhanced stability of the M@Cu SAA during catalytic reactions.

As shown in Figure 2A, the majority of the dissolution potential values are positive, indicating the favorable stability of M@Cu SAAs at negative applied potentials during CO₂RR. We noted that the dissolution potential is determined in an acid aqueous solution at pH = 0.

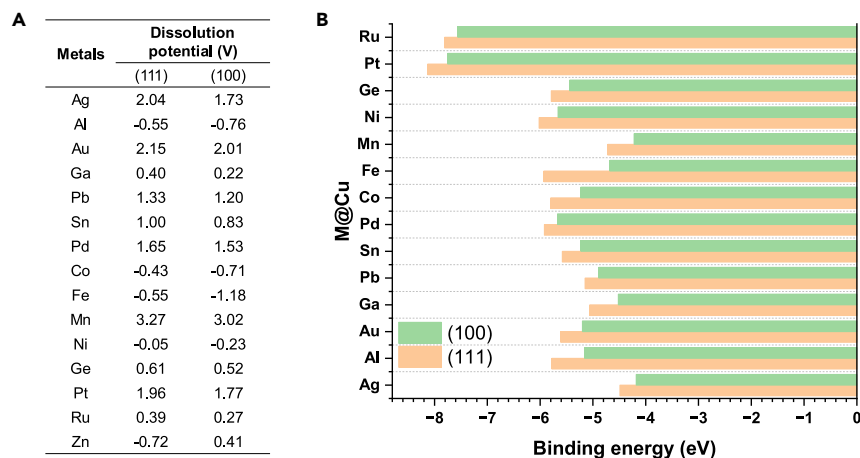


Figure 2. The measurement of M@Cu stability

(A and B) (A) The dissolution potential (U_{dis} , V vs. SHE) for $M + nH^+ \rightarrow M^{n+} + n/2H_2$ at pH = 0, and (B) binding energy of M (E_B , eV) on M@Cu(111) and (100) surfaces.

Experimentally, alkaline electrolytes are commonly used for CO₂RR, which provides an additional protection against metal dissolution.³² Regarding the binding energy of M in the M@Cu SAAs, the negative values (excluding Zn) indicate the formation of stable configurations (Figure 2B). This indicates that the M atoms have a favorable affinity with the Cu surface, forming robust M@Cu structures. Furthermore, we observed that the M@Cu (111) surface generally exhibits higher stability compared to the (100) surface, which can be attributed to the lower surface energy of Cu(111) compared to Cu(100).³³ We noted that tuning their stacking fault energy is crucial for the formation of dislocations and defects at room temperature leading to recrystallization, which requires finely controlling annealing process for the grain structure.³⁴ Moreover, external factors such as grain boundaries and vacancies are also relevant, imposing requirements on conditions like temperature control during the synthesis process.³⁵ There are reports that in the chemical reaction process, doping atoms on Cu-based single-atom catalysts can segregate at kink positions.³⁶ The adsorption of reaction intermediates also plays a role in this segregation.³⁷ However, an in-depth exploration of all influencing factors goes beyond the scope of this article. By considering both the negative binding energy values and the relative stability of the M@Cu, we conclude that M@Cu SAAs have the potential to form stable structures for CO₂RR.

Classification of active sites

We began the investigation by examining the adsorption site of *CO, as *CO plays a central role in the formation of C₁ and C₂ products in CO₂RR.^{38–40} *CO can directly desorb from surface as CO product, while CH₄, CH₃OH are formed from further *CO reduction.^{41,42} Moreover, the adsorption energy of *CO holds great significance in determining the reaction barriers in CO₂RR.^{43,44} We find that on Cu(111) surface, the most stable adsorption site for *CO is the 3-fold hollow site, with an adsorption energy of -0.59 eV. In contrast, the bridge site exhibits a relatively weaker adsorption energy of -0.55 eV, while the top site shows even weaker adsorption with an energy of -0.45 eV. On Cu(100) surface, the adsorption of *CO on the hollow site is also stronger compared to the adsorption on the bridge site and top site (Figure S1). For M@Cu, we found that *CO that is initially placed on the bridge site tends to migrate to either the top site of M or the hollow site. The site on top of M is denoted as T1, and the hollow site adjacent to M and around copper in vicinity are denoted as H1 and H2. (Figure S1) Therefore, comparing the adsorption energy of *CO on the top site of M (T1) and hollow site (H1 and H2) allows for identification of preferred site. As shown in Figures 3A and 3B, the most stable adsorption sites are classified into two groups: on Ag, Al, Au, Ge, Ga, Pb, Si, Sn@Cu adsorption site is H2, denoted as AD mode. On Fe, Ru, Pd, Co, Ni, Pt@Cu, the strongest adsorption site is T1, denoted as SE mode (Figures 2C–2R, S2, and S3). On Mn@Cu(111) the favorable site is H1 site which could be considered as AD mode, and Mn@Cu(100) the favorable site is T1 site with SE mode. We can see for Al, Si, Ga, Ge, Sn, Pb, and d-block elements with full d-shell Ag (4d¹⁰ 5s¹), Au (5d¹⁰ 6s¹), M@Cu are more likely to form AD mode for adsorption, while d-block elements with open d-shell such as Co (3d⁷ 4s²), Fe (3d⁶ 4s²), Ni (3d⁸ 4s²), Pt (5d⁹ 6s¹), and Ru (4d⁷ 5s¹), M@Cu tends to form SE mode. We noted that on Co, Fe, Pt, Ru@Cu on (111) surface and Co, Fe, Ni, Ru@Cu on (100) surface, the *CO species initially placed on H1 site moves to T1 site after optimization. We further studied the relation between d-band center and *CO adsorption energy. As shown in Figure S4, the linear fitting relation indicates that the closer of the d-band center to the Fermi level, the stronger the *CO adsorption. It indicates that the electronic structure of M is crucial for the adsorption of *CO on M@Cu.^{45,46}

The effects of solvent are investigated using VASPsol on Fe, Co, Mn, Au, Al, Sn@Cu (111) SAAs (Figure S5). The Fe@Cu and Co@Cu still exhibits the strongest adsorption on top site on Fe and Co atoms (SE mode), respectively. On Mn@Cu the favorable site is the H1 site. On the other hand, Au, Al, Sn@Cu demonstrates a favorable adsorption on H2 site (AD mode). We further studied the cation effect on Fe@Cu and Sn@Cu SAAs. As shown in Figure S6, the favorable sites are still T1 and H2 for Fe@Cu and Sn@Cu, respectively. The results show that the solvent and cation do not change the adsorption mode for M@Cu. Moreover, we investigated the adsorption site for *COOH, and the results

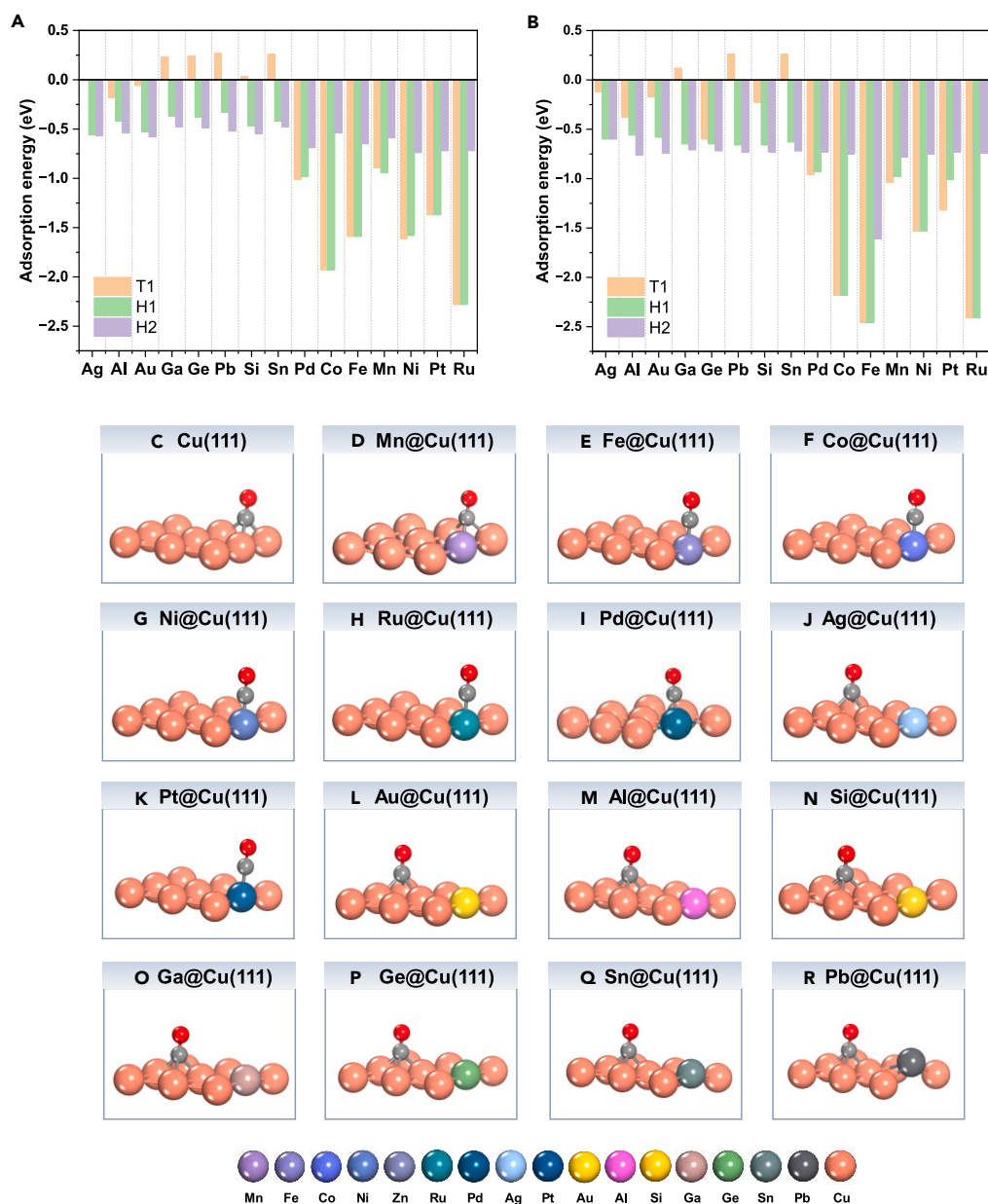


Figure 3. The adsorption energy of *CO on M@Cu and corresponding configurations

(A and B) (A) Adsorption energy on M@Cu(111) and (B) (100) surfaces.

(C–R) The *CO adsorption configurations on M@Cu(111).

are similar to that of *CO (Figures S7 and S8). On M@Cu with AD adsorption mode, the carbon and oxygen atoms of *CO intermediate bind to the copper atom adjacent to secondary element M. However, on M@Cu with SE mode, *COOH adsorbs with carbon binding on secondary element M and oxygen on copper. For *OCOH, the adsorption sites are similar for all catalysts, with oxygen binding on the secondary element M and carbon binding on copper (Figures S9 and S10).

We noted that the CO adsorption is mainly attributed to the top and bridge site in lots of experimental works. Using *in situ* Fourier transform infrared spectroscopy (FTIR) characterization, the peak around 1850 cm^{-1} to 1950 cm^{-1} was attributed to bridge configuration, and the peak around 2000 cm^{-1} to 2100 cm^{-1} was attributed to atop configuration.^{47–49} However, it should be noted that the distinction between bridge and hollow configuration can be very small. The peak between 1800 cm^{-1} to 1900 cm^{-1} could be the multi-bond bridge or hollow configurations.⁵⁰ Our group found that the peak around 1790 cm^{-1} can be attributed to hollow site.⁵¹ The peaks corresponding to the bridge and atop configurations in FTIR can be very close, making it difficult to clearly distinguish between them. Furthermore, several theoretical

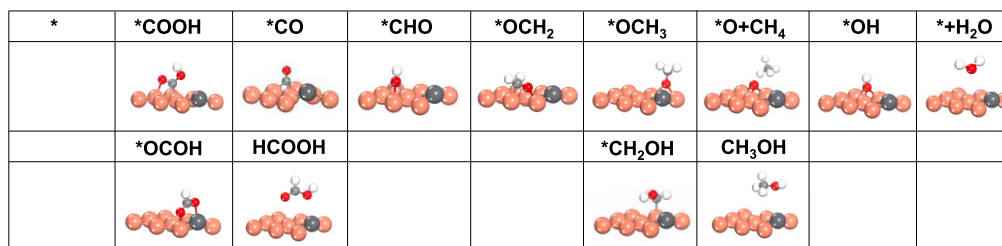


Figure 4. Key intermediates in CO₂RR

calculations works found that hollow configuration is the most stable comparing to top and bridge.^{52–54} Therefore, there is precedent in experimental research for studying hollow sites, and the preferential adsorption of hollow site sites has been confirmed by a series of studies, thus substantiating the validity of our research.

CO and HCOOH production

We conducted an investigation into the formation of key intermediates, as shown in Figure 4, in order to depict free energy profiles for C1 products on M@Cu SAAs. CO and HCOOH are commonly reported as two-electron reduction products in studies on SAAs. In Figure 5A, it is evident that M@Cu with the AD mode shows a lower affinity for *CO compared to Cu, while M@Cu with the SE mode exhibits stronger *CO adsorption than Cu. However, on Co, Fe, Ni, Pt, and Ru@Cu, *CO adsorption is excessively strong, hindering the desorption of CO products from the catalyst surface. On Al, Mn, and Si@Cu, CO production is improved compared to Cu. The improvement could be attributed to the lower energy barrier for *COOH formation, and a suitable *CO binding energy for CO products to desorb. As for HCOOH production in Figure 5B, HCOOH is more facile to form on Ag, Au, Ge, Pb, Pd, Sn, Pt@Cu, which exhibits a more suitable energy for *OCOH energy comparing to Cu. Specifically, Mn@Cu(111) exhibits the lowest energy barrier of 0.44 eV for CO products, and Pb@Cu(111) demonstrates the lowest energy barrier of 0.26 eV for HCOOH products. As shown in Figures 5C and 5D that on M@Cu(100) surface, Ag, Ga, Ge, Al, Si@Cu show high

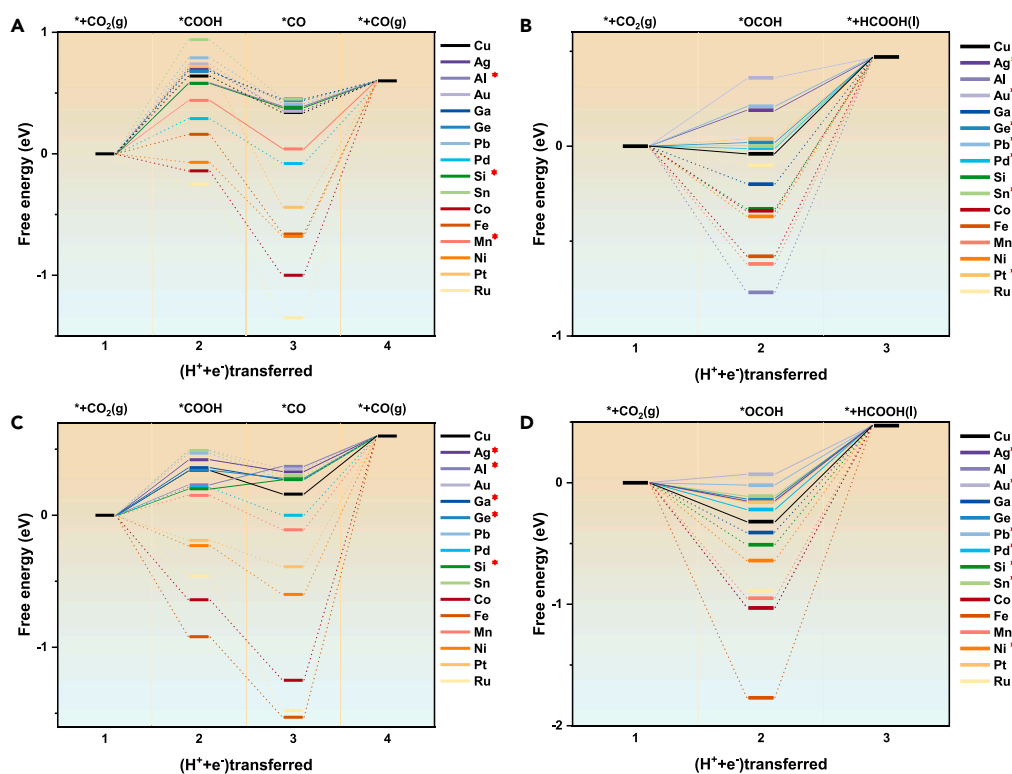


Figure 5. The free energy profile of CO₂RR toward CO product

(A–D) (A) M@Cu(111), (C) M@Cu(100) surface, and HCOOH product on (B) M@Cu (111), (D) M@Cu (100) surface. Noted that comparing to copper catalyst, the M@Cu catalysts with a lower energy barrier for potential-determining step (PDS) than Cu are denoted with asterisk.

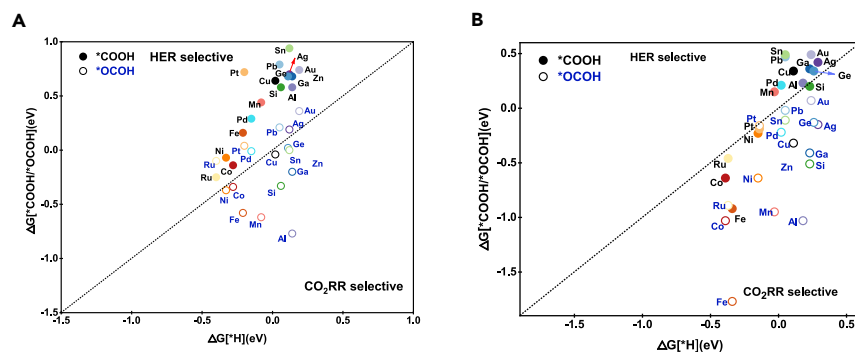


Figure 6. The comparison between CO₂RR and HER

(A and B) The Gibbs-free energy change of CO₂RR versus HER at 0 V (vs. RHE) on (A) M@Cu(111) and (B) M@Cu(100).

activity for CO, and Ag, Au, Pb, Pd, Si, Sn, Ni@Cu for HCOOH. Specifically, Al@Cu(100) exhibits the lowest energy barrier of 0.23 eV for CO, and Au@Cu(100) shows the lowest energy barrier of 0.40 eV for HCOOH. Pb@Cu with the lowest energy barrier for HCOOH product is consistent with the recent discovery showing that Pb-Cu alloy is an efficient catalyst for HCOOH production.⁵

Hydrogen evolution reaction

Additionally, we studied the parasite hydrogen evolution reaction (HER), which is a typical competing reaction that captures protons. The initial protonation step of CO₂RR leads to *COOH or *OCOH, while HER is initialized with *H formation on catalyst surface. It could be seen in Figure 6 that most of the points lie below the parity line on Cu(100). On Cu(111), the points for *COOH intermediate locate above the parity line, while points for *OCOH are mostly below the parity line. It indicates that HER is more inclined to occur on Cu(111) comparing to Cu(100). The experimental studies suggest a potential-dependent intermediate formation, with *COOH formation at more negative potential. This trend is in line with the relative energy of *COOH and *OCOH.⁵⁵ To suppress HER, practical approaches involve the use of alkaline electrolytes and gas diffusion electrodes to enhance the mass transport of CO₂. These strategies help suppress the HER and promote the desired CO₂RR.⁴¹

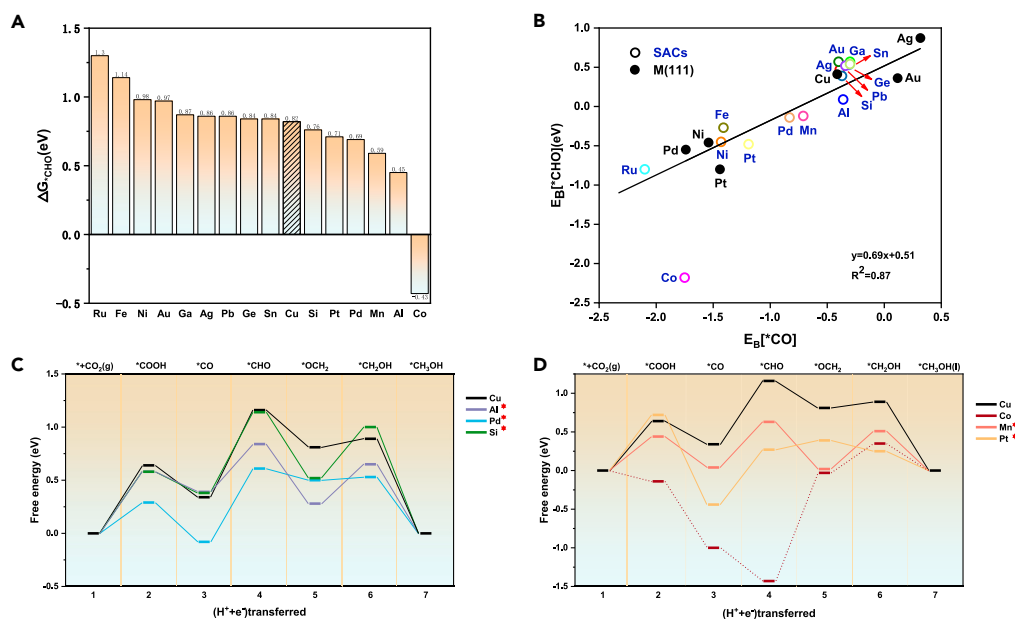


Figure 7. The CH₃OH and CH₄ production on M@Cu

(A) The energy barrier of *CO → *CHO on M@Cu(111).

(B) The correlation relationship between *CHO and *CO on M(111) surface and M@Cu catalysts.

(C and D) The energy profile for CH₃OH formation on M@Cu(111) for (C) Al, Pd, Si, and (D) Co, Mn, Pt@Cu. The catalysts with a lower energy barrier for PDS than copper are marked with asterisk.

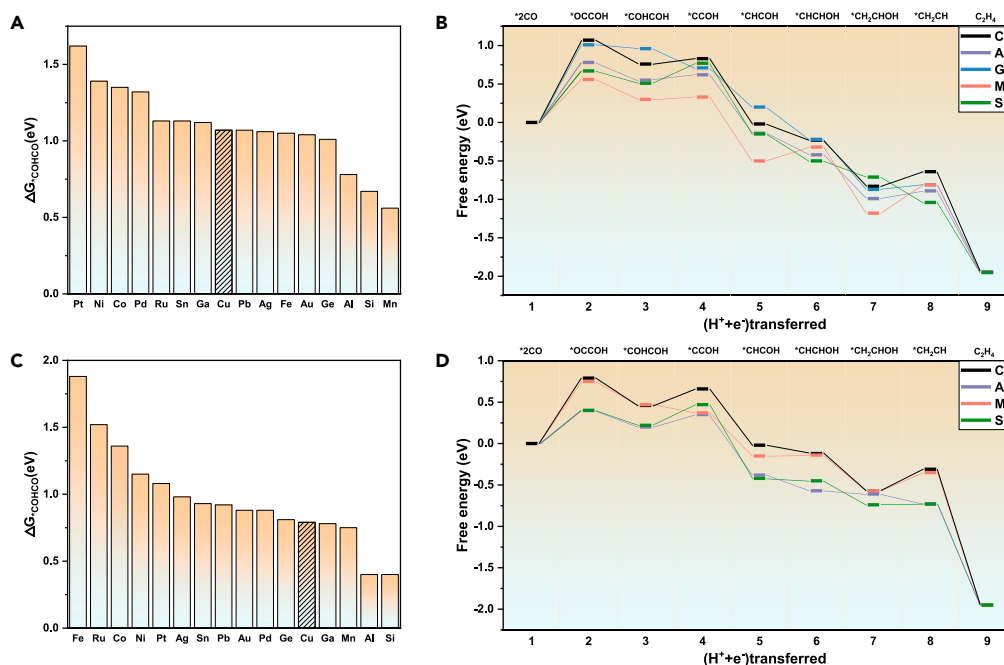


Figure 8. The C₂ production on M@Cu catalysts

(A–D) The energy barrier of *OCCOH formation and corresponding energy profile for C₂H₄ formation on (A and B) M@Cu(111) and (C and D) M@Cu(100).

CH₃OH and CH₄ production

The reduction of *CO to *CHO is a critical step in the formation of deep reduction products such as CH₃OH and CH₄, and it is known to be energetically demanding.⁵⁵ We investigated the energy barrier of *CO → *CHO on M@Cu as shown in Figure 7A. Si, Pt, Pd, Mn, Al, Co@Cu exhibit higher activity compared to Cu. Similarly, on the M@Cu(100) surface, Pd, Au, Pb, Sn, Si, Mn, Al@Cu catalysts demonstrate lower energy barriers than pure Cu (Figure S11). We presented the energy profile on the M@Cu(111) as shown in Figures 7C and 7D, respectively. It is evident that M@Cu with AD mode (Al, Si) generally exhibits higher activity, primarily due to the lower energy barrier of the potential-determining step (PDS) of *CO to *CHO. Al, Pd, Si, Pt, Mn@Cu exhibit better activity than copper catalyst for CH₃OH production, and the trend is consistent for CH₄ production (Figure S12). For M@Cu(100), we found a comparable trend with better activity on M@Cu with AD mode than SE mode (Figures S13–S17). It is evident for the importance of the adsorption mode in modulating the activity for CH₃OH and CH₄.

We further investigated the scaling relations between *CO and *CHO binding energy on both pure metal and M@Cu (111) surface, as depicted in Figure 7B. Interestingly, we observed that comparing to Cu, Al@Cu, Si@Cu catalysts exhibit a stronger *CHO adsorption, and a weaker adsorption for *CO. This combination leads to a decrease in the energy barrier for the *CO to *CHO conversion, which is the crucial step in the formation of deep reduction products. According to Nørskov et al., the volcano plot analysis among transition-metal catalysts suggests that crystalline Cu is positioned near the peak for *CO binding energy, on the strong-binding side of the volcano curve. This positioning implies that copper possesses an optimal *CO binding capability for facilitating deep reduction products in catalytic reactions.⁴³ Herein, it is intriguing that the activity of copper catalysts can be enhanced by moderately weakening the binding strength of *CO, while enhancing the adsorption of *CHO by incorporating p-block elements into the M@Cu catalysts. This phenomenon highlights the flexibility of *CO and *CHO adsorption on M@Cu. Specifically, *CO binding can be regulated in the opposite direction to *CHO on certain M@Cu, which means that by tuning the catalyst composition, we can selectively weaken the binding of *CO while simultaneously enhance the binding of *CHO. This nuanced tuning of *CO and *CHO binding on M@Cu deepens our understanding into the volcano descriptors and scaling relations which greatly influences the catalytic performance.

C₂ production on M@Cu catalysts

For the formation of C₂ products, we focus on the C-C coupling step of 2*CO+*H → *OCCOH, which is known to be the most energetically demanding step for C₂ product.⁴⁰ As shown in Figures 8A and 8C, we observe that on Al, Mn, and Si@Cu, the Gibbs-free energy barrier for 2*CO → *OCCOH is significantly lower compared to copper catalysts on both (111) and (100) surfaces (Figures S18 and S19). Additionally, we find that Ge@Cu on (111) surface also exhibits a favorable *OCCOH formation. As shown in Figures 8B and 8D, the energy profiles indicate that the following steps after the formation of *OCCOH are relatively energetically easy (Figures S20 and S21). We also investigated the relationship between C₂ activity and C₂/C₁ selectivity (Figure S22), which shows that Si@Cu and Al@Cu are the most active and selective for C₂ products. We noted that there are research demonstrating that Al and Si are effective in facilitating the formation of an interface with favorable

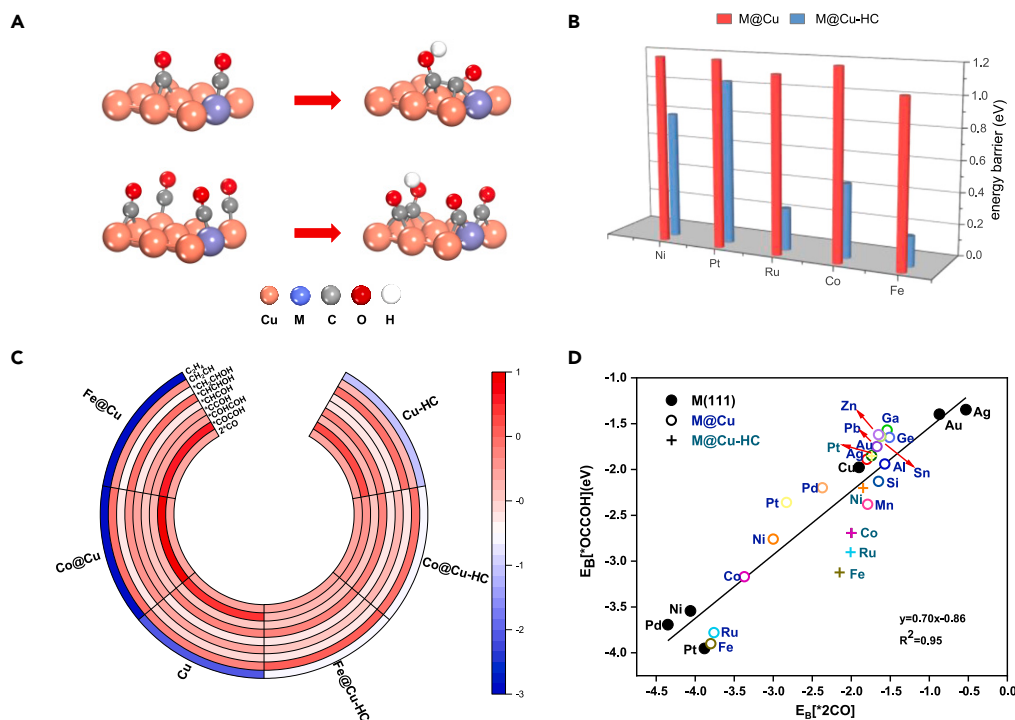


Figure 9. The *CO coverage effect for C₂ production

(A) The schematic illustration of C-C coupling reaction with 0/9 and 2/9 coverage of *CO.

(B) The C-C coupling reaction barrier with *CO coverage of 0/9 and 2/9 (denoted as -HC).

(C and D) (C) The heatmap of energy barrier for the formation of intermediates in C₂H₄ on Cu, Co@Cu, Fe@Cu, and counterparts with high coverage of 2/9 (-HC),

(d) the scaling relation of binding energy of *OCCOH and *2CO on M(111) and M@Cu.

coordination environment, ultimately enhancing C-C dimerization processes. These experimental findings are in agreement with the computational results obtained in our study.^{15,56}

As mentioned previously, catalysts with AD adsorption mode generally exhibit a higher favorability for C-C coupling compared to catalysts with SE mode. However, there have been several reports of effective Co@Cu and Pd@Cu catalysts, despite the dominance of SE adsorption mode. These observations raise questions regarding the mechanisms underlying the performance of these catalysts and warrant further investigation.^{16,22} On the other hand, the effect of *CO coverage on CO₂RR performance has been demonstrated as a key factor.^{14,57} We studied C-C coupling reaction for SE adsorption with *CO coverage of 0/9 (no extra *CO) and 2/9 (two extra *CO). As shown in Figure 9A. Interestingly, we found at high *CO coverage, the active sites are relocated to the copper adjacent to secondary elements. In Figure 9B, the C-C coupling reaction with high coverage is much improved comparing to low *CO coverage, with Co@Cu, Fe@Cu and Ru@Cu exhibiting energy barriers lower than 0.4 eV. We further investigate the energy profile of C₂H₄ formation on Cu, Co@Cu, and Fe@Cu catalysts under low and high *CO coverage. As shown Figure 9C, the energy barrier for C₂H₄ production decreases by 0.51 eV and 0.92 eV for Co@Cu and Fe@Cu compared to pure Cu, respectively. Notably, on Co@Cu and Fe@Cu, the formation of *COCOCH is significantly improved, leading to a change in the potential-determining step (PDS) from *COCOCH formation at low *CO coverage to *CH₂CH formation at high *CO coverage. High *CO coverage results in a stronger interaction between *CO, which can potentially lower the energy barrier for C-C coupling. However, in Figure 9C, only limited improvement is observed in the C-C coupling reaction on Cu at high *CO coverage, suggesting that the decreased energy barrier observed on Co@Cu and Fe@Cu is primarily due to the active site relocation rather than the enhanced *CO adsorbate-adsorbate interaction (Figures S23 and S24). At high *CO coverage on M@Cu catalysts, the M site is already adsorbed with *CO, leaving no available sites for additional *CO. Consequently, the newly introduced *CO molecules adsorb on the copper sites adjacent to the secondary elements. Remarkably, these newly formed *CO species exhibit a moderate binding strength on M@Cu, which leads to a decrease in the energy barrier for the C-C coupling reaction.

To further understand the relation between activity and *CO coverage, we correlated the binding energy of *OCCOH and *2CO as shown Figure 9D. A linear relation on M(111) surface was observed between these two binding energies. However, we discover that Al@Cu, Mn@Cu, Ge@Cu and Si@Cu deviated from this linearity, showing weaker *CO binding and stronger *OCCOH binding. On the other hand, Fe@Cu and Ru@Cu, which exhibited inferior performance, also deviated from the linearity but were located far from the copper position. Therefore, to achieve high activity, the catalysts should exhibit a moderate deviation from the scaling relation, with reasonably weaker *CO binding and stronger *OCCOH binding. This nuanced tuning of the binding energies is crucial for optimizing the catalytic performance in the C-C

coupling reaction. Consistently, our results demonstrate that at high *CO coverage, Co@Cu-HC, Fe@Cu-HC, Ni@Cu-HC, and Ru@Cu-HC catalysts exhibit a favorable and suitable deviation from the scaling relation by shifting the active site to the copper. This observation provides a plausible explanation for the improved C-C coupling activity at high *CO coverage. By deviating from the scaling relation in the favorable direction, the C-C coupling process is effectively improved for C_2 production.

Conclusion

In summary, by investigating the correlation between the electronic structures of secondary element and energy profiles, we provide a detailed picture of CO_2RR over copper-based SAAs catalysts. M@Cu with AD mode is generally more active than the ones with SE mode, which is attributed to that AD mode leads to a moderate deviation of linear scaling relation. As for C_2 products, Al@Cu, Si@Cu with the AD mode exhibit higher activity for C-C coupling reaction. Achieving a suitable deviation from the linear scaling relation in the vicinity of pure Cu catalyst is crucial for reducing the barrier of key reaction steps. Additionally, at high *CO coverage, the active site shifts to the copper atoms adjacent to the secondary element on Co, Fe, Ni, Ru@Cu, resulting in enhanced activity for the C-C coupling reaction. We found that the primary function of secondary element M is assisting copper to adsorb *CO moderately weaker while improved *CHO and *COCOH adsorption. We believe this work provides valuable insights into the manipulation of electronic structure, adsorption modes, and scaling relations to achieve highly active SAAs catalysts for CO_2RR .

Limitations of the study

The present work is a theoretical study on Cu SAAs for CO_2RR . The active sites are predicted using binding of key intermediates, and a comprehensive simulation is presented to gain more knowledge of the mechanical picture of CO_2RR on various Cu SAAs. Some interesting behavior of active sites on Cu SAAs is uncovered which is correlated to the secondary elements and *CO coverage. However, it is essential to acknowledge that the stability of Cu SAAs is a concern in electrochemical reactions. The surface structure of SAAs may undergo significant reconstruction, potentially influencing the electronic structure and activity of Cu SAAs. This reconstruction is not considered in the current work. We also note that the absolute values of calculations are dependent on the PBE functional in DFT software.

STAR★METHODS

Detailed methods are provided in the online version of this paper and include the following:

- KEY RESOURCES TABLE
- RESOURCE AVAILABILITY
 - Lead contact
 - Materials availability
 - Data and code availability
- METHOD DETAILS

SUPPLEMENTAL INFORMATION

Supplemental information can be found online at <https://doi.org/10.1016/j.isci.2023.107953>.

ACKNOWLEDGMENTS

This work was supported by the National Natural Science Foundation of China (22002158, 22172009, 22125205, 92045302), the 'Transformational Technologies for Clean Energy and Demonstration' Strategic Priority Research Program of the Chinese Academy of Sciences (XDA21070613), the CAS Youth Innovation Promotion (Y201938) and the Photon Science Center for Carbon Neutrality.

AUTHOR CONTRIBUTIONS

T.L. and G.S. performed the computation. T.L. and G.S. wrote the manuscript. G.W. and T.L. designed the project and revised the manuscript. Y.S., Q.W., X.L., Z.C., and Z.P. revised the manuscript. All authors were involved in the general discussion. The manuscript was written through contributions of all authors. All authors have given approval to the final version of the manuscript.

DECLARATION OF INTERESTS

The authors declare no competing interests.

Received: June 28, 2023

Revised: July 17, 2023

Accepted: September 14, 2023

Published: September 19, 2023

REFERENCES

- Appel, A.M., Bercaw, J.E., Bocarsly, A.B., Dobbek, H., DuBois, D.L., Dupuis, M., Ferry, J.G., Fujita, E., Hille, R., Kenis, P.J.A., et al. (2013). Frontiers, Opportunities, and Challenges in Biochemical and Chemical Catalysis of CO₂ Fixation. *Chem. Rev.* 113, 6621–6658. <https://doi.org/10.1021/cr300463y>.
- Nitopi, S., Bertheussen, E., Scott, S.B., Liu, X., Engstfeld, A.K., Horch, S., Seger, B., Stephens, I.E.L., Chan, K., Hahn, C., et al. (2019). Progress and Perspectives of Electrochemical CO₂ Reduction on Copper in Aqueous Electrolyte. *Chem. Rev.* 119, 7610–7672. <https://doi.org/10.1021/acs.chemrev.8b00705>.
- Qiao, J., Liu, Y., Hong, F., and Zhang, J. (2014). A Review of Catalysts for the Electroreduction of Carbon Dioxide to Produce Low-Carbon Fuels. *Chem. Soc. Rev.* 43, 631–675. <https://doi.org/10.1039/C3CS60323G>.
- Lee, M.Y., Park, K.T., Lee, W., Lim, H., Kwon, Y., and Kang, S. (2019). Current Achievements and the Future Direction of Electrochemical CO₂ Reduction: A Short Review. *Crit. Rev. Environ. Sci. Technol.* 50, 769–815. <https://doi.org/10.1080/10643389.2019.1631991>.
- Zheng, T., Liu, C., Guo, C., Zhang, M., Li, X., Jiang, Q., Xue, W., Li, H., Li, A., Pao, C.W., et al. (2021). Copper-Catalysed Exclusive CO₂ to Pure Formic Acid Conversion Via Single-Atom Alloying. *Nat. Nanotechnol.* 16, 1386–1393. <https://doi.org/10.1038/s41565-021-00974-5>.
- Luo, W., Xie, W., Mutschler, R., Oveisi, E., De Gregorio, G.L., Buonsanti, R., and Züttel, A. (2018). Selective and Stable Electroreduction of CO₂ to CO at the Copper/Indium Interface. *ACS Catal.* 8, 6571–6581. <https://doi.org/10.1021/acscatal.7b04457>.
- Peterson, A.A., Abild-Pedersen, F., Studt, F., Rossmeisl, J., and Nørskov, J.K. (2010). How Copper Catalyzes the Electroreduction of Carbon Dioxide into Hydrocarbon Fuels. *Energy Environ. Sci.* 3, 1311. <https://doi.org/10.1039/C0EE00071J>.
- Montoya, J.H., Peterson, A.A., and Nørskov, J.K. (2013). Insights into C-C Coupling in CO₂ Electroreduction on Copper Electrodes. *ChemCatChem* 5, 737–742. <https://doi.org/10.1002/cctc.201200564>.
- Gauthier, J.A., Stenlid, J.H., Abild-Pedersen, F., Head-Gordon, M., and Bell, A.T. (2021). The Role of Roughening to Enhance Selectivity to C₂₊ Products During CO₂ Electroreduction on Copper. *ACS Energy Lett.* 6, 3252–3260. <https://doi.org/10.1021/acscenergylett.1c01485>.
- Pérez-Gallent, E., Marcandalli, G., Figueiredo, M.C., Calle-Vallejo, F., and Koper, M.T.M. (2017). Structure- and Potential-Dependent Cation Effects on CO Reduction at Copper Single-Crystal Electrodes. *J. Am. Chem. Soc.* 139, 16412–16419. <https://doi.org/10.1021/jacs.7b10142>.
- Pedersen, J.K., Batchelor, T.A.A., Bagger, A., and Rossmeisl, J. (2020). High-Entropy Alloys as Catalysts for the CO₂ and CO Reduction Reactions. *ACS Catal.* 10, 2169–2176. <https://doi.org/10.1021/acscatal.9b04343>.
- Hao, J., Zhuang, Z., Hao, J., Cao, K., Hu, Y., Wu, W., Lu, S., Wang, C., Zhang, N., Wang, D., et al. (2022). Strain Relaxation in Metal Alloy Catalysts Steers the Product Selectivity of Electrocatalytic CO₂ Reduction. *ACS Nano* 16, 3251–3263. <https://doi.org/10.1021/acsnano.1c11145>.
- Ye, K., Cao, A., Shao, J., Wang, G., Si, R., Ta, N., Xiao, J., and Wang, G. (2020). Synergy Effects on Sn-Cu Alloy Catalyst for Efficient CO₂ Electroreduction to Formate with High Mass Activity. *Sci. Bull.* 65, 711–719. <https://doi.org/10.1016/j.scib.2020.01.020>.
- Wang, X., Ou, P., Wicks, J., Xie, Y., Wang, Y., Li, J., Tam, J., Ren, D., Howe, J.Y., Wang, Z., et al. (2021). Gold-in-Copper at Low *CO Coverage Enables Efficient Electromethanation of CO₂. *Nat. Commun.* 12, 3387. <https://doi.org/10.1038/s41467-021-23699-4>.
- Zhong, M., Tran, K., Min, Y., Wang, C., Wang, Z., Dinh, C.T., De Luna, P., Yu, Z., Rasouli, A.S., Brodersen, P., et al. (2020). Accelerated Discovery of CO₂ Electrocatalysts Using Active Machine Learning. *Nature* 581, 178–183. <https://doi.org/10.1038/s41586-020-2242-8>.
- Xie, Y., Ou, P., Wang, X., Xu, Z., Li, Y.C., Wang, Z., Huang, J.E., Wicks, J., McCallum, C., Wang, N., et al. (2022). High Carbon Utilization in CO₂ Reduction to Multi-Carbon Products in Acidic Media. *Nat. Catal.* 5, 564–570. <https://doi.org/10.1038/s41929-022-00788-1>.
- Guo, X., Zhang, Y., Deng, C., Li, X., Xue, Y., Yan, Y.M., and Sun, K. (2015). Composition Dependent Activity of Cu-Pt Nanocrystals for Electrochemical Reduction of CO₂. *Chem. Commun.* 51, 1345–1348. <https://doi.org/10.1039/C4CC08175G>.
- Ren, D., Ang, B.S.H., and Yeo, B.S. (2016). Tuning the Selectivity of Carbon Dioxide Electroreduction toward Ethanol on Oxide-Derived Cu₂Zn Catalysts. *ACS Catal.* 6, 8239–8247. <https://doi.org/10.1021/acscatal.6b02162>.
- Morimoto, M., Takatsujii, Y., Yamasaki, R., Hashimoto, H., Nakata, I., Sakakura, T., and Haruyama, T. (2017). Electrodeposited Cu-Sn Alloy for Electrochemical CO₂ Reduction to CO/HCOO⁻. *Electrocatalysis* 9, 323–332. <https://doi.org/10.1007/s12678-017-0434-2>.
- Sarfraz, S., Garcia-Esparza, A.T., Jedidi, A., Cavallo, L., and Takanabe, K. (2016). Cu-Sn Bimetallic Catalyst for Selective Aqueous Electroreduction of CO₂ to CO. *ACS Catal.* 6, 2842–2851. <https://doi.org/10.1021/acscatal.6b00269>.
- Li, M., Wang, J., Li, P., Chang, K., Li, C., Wang, T., Jiang, B., Zhang, H., Liu, H., Yamauchi, Y., et al. (2016). Mesoporous Palladium-Copper Bimetallic Electrodes for Selective Electrocatalytic Reduction of Aqueous CO₂ to CO. *J. Mater. Chem. A* 4, 4776–4782. <https://doi.org/10.1039/C6TA00487C>.
- Bernal, M., Bagger, A., Scholten, F., Sinev, I., Bergmann, A., Ahmadi, M., Rossmeisl, J., and Cuenya, B.R. (2018). CO₂ Electroreduction on Copper-Cobalt Nanoparticles: Size and Composition Effect. *Nano Energy* 53, 27–36. <https://doi.org/10.1016/j.nanoen.2018.08.027>.
- Bagger, A., Ju, W., Varela, A.S., Strasser, P., and Rossmeisl, J. (2017). Electrochemical CO₂ Reduction: A Classification Problem. *ChemPhysChem* 18, 3266–3273. <https://doi.org/10.1002/cphc.201700736>.
- Nørskov, J.K., Bliigaard, T., Logadottir, A., Kitchin, J.R., Chen, J.G., Pandelov, S., and Stimming, U. (2005). Trends in the Exchange Current for Hydrogen Evolution. *J. Electrochem. Soc.* 152, J23. <https://doi.org/10.1149/1.1856988>.
- Wang, Y., Han, P., Lv, X., Zhang, L., and Zheng, G. (2018). Defect and Interface Engineering for Aqueous Electrocatalytic CO₂ Reduction. *Joule* 2, 2551–2582. <https://doi.org/10.1016/j.joule.2018.09.021>.
- Chen, Z., and Zhang, P. (2022). Electronic Structure of Single-Atom Alloys and Its Impact on the Catalytic Activities. *ACS Omega* 7, 1585–1594. <https://doi.org/10.1021/acsomega.1c06067>.
- Greiner, M.T., Jones, T.E., Beeg, S., Zwiener, L., Scherzer, M., Girgsdies, F., Piccinin, S., Armbrüster, M., Knop-Gericke, A., and Schlögl, R. (2018). Free-Atom-Like d States in Single-Atom Alloy Catalysts. *Nat. Chem.* 10, 1008–1015. <https://doi.org/10.1038/s41557-018-0125-5>.
- Darby, M.T., Réocreux, R., Sykes, E.C.H., Michaelides, A., and Stamatakis, M. (2018). Elucidating the Stability and Reactivity of Surface Intermediates on Single-Atom Alloy Catalysts. *ACS Catal.* 8, 5038–5050. <https://doi.org/10.1021/acscatal.8b00881>.
- Luo, W., Nie, X., Janik, M.J., and Asthagiri, A. (2015). Facet Dependence of CO₂ Reduction Paths on Cu Electrodes. *ACS Catal.* 6, 219–229. <https://doi.org/10.1021/acscatal.5b01967>.
- Kim, S.J., Chung, S.P., Gil, H.W., Choi, S.C., Kim, H., Kang, C., Kim, H.J., Park, J.S., Lee, K.W., Cho, J., et al. (2016). Mechanism of the Surface Hydrogen Induced Conversion of CO₂ to Methanol at Cu(111) Step Sites. *ACS Catal.* 31, 1037–1041. <https://doi.org/10.1021/acscatal.5b02083>.
- Schouten, K.J.P., Qin, Z., Pérez Gallent, E., and Koper, M.T.M. (2012). Two Pathways for the Formation of Ethylene in CO Reduction on Single-Crystal Copper Electrodes. *J. Am. Chem. Soc.* 134, 9864–9867. <https://doi.org/10.1021/acscatal.5b02083>.
- Sang, J., Wei, P., Liu, T., Lv, H., Ni, X., Gao, D., Zhang, J., Li, H., Zang, Y., Yang, F., et al. (2022). A Reconstructed Cu₂P₂O₇ Catalyst for Selective CO₂ Electroreduction to Multicarbon Products. *Angew. Chem. Int. Ed.* 61, e202114238. <https://doi.org/10.1002/anie.202114238>.
- Fishman, M., Zhuang, H.L., Mathew, K., Dirschka, W., and Hennig, R.G. (2013). Accuracy of Exchange-Correlation Functionals and Effect of Solvation on the Surface Energy of Copper. *Phys. Rev. B* 87, 245402. <https://doi.org/10.1103/PhysRevB.87.245402>.
- Freudenberger, J., Kauffmann, A., Klauß, H., Marr, T., Nenkov, K., Subramanya Sarma, V., and Schultz, L. (2010). Studies on Recrystallization of Single-phase Copper Alloys by Resistance Measurements. *Acta Mater.* 58, 2324–2329. <https://doi.org/10.1016/j.actamat.2009.12.018>.
- Subramanya Sarma, V., Sivaprasad, K., Sturm, D., and Heilmaier, M. (2008). Microstructure and Mechanical Properties of Ultra Fine Grained Cu-Zn and Cu-Al Alloys Produced by Cryorolling and Annealing. *Mater. Sci. Eng. A* 489, 253–258. <https://doi.org/10.1016/j.msea.2007.12.016>.
- Han, J.W., Kitchin, J.R., and Sholl, D.S. (2009). Step Decoration of Chiral Metal Surfaces. *J. Chem. Phys.* 130, 124710. <https://doi.org/10.1063/1.3096964>.
- Menning, C.A., and Chen, J.G. (2008). Thermodynamics and Kinetics of

- Oxygen-induced Segregation of 3d Metals in Pt-3d-Pt (111) and Pt-3d-Pt (100) Bimetallic Structures. *J. Chem. Phys.* **128**, 164703. <https://doi.org/10.1063/1.2900962>.
38. Luo, T., Liu, K., Fu, J., Chen, S., Li, H., Pan, H., and Liu, M. (2023). Electric Double Layer Structure in Electrocatalytic Carbon Dioxide Reduction. *Adv. Energy Sustain. Res.* **4**, 2200148. <https://doi.org/10.1002/aesr.202200148>.
39. Wang, X.Q., Chen, Q., Zhou, Y.J., Li, H.M., Fu, J.W., and Liu, M. (2022). Cu-based bimetallic catalysts for CO₂ reduction reaction. *Adv. Sens. Energy Mater.* **1**, 100023. <https://doi.org/10.1016/j.asems.2022.100023>.
40. Luo, T., Liu, K., Fu, J., Chen, S., Li, H., Hu, J., and Liu, M. (2022). Tandem catalysis on adjacent active motifs of copper grain boundary for efficient CO₂ electroreduction toward C₂ products. *J. Energy Chem.* **70**, 219–223. <https://doi.org/10.1016/j.jechem.2022.02.050>.
41. Hori, Y., Murata, A., and Yoshinami, Y. (1991). Adsorption of CO, Intermediately Formed in Electrochemical Reduction of CO₂, at a Copper Electrode. *Faraday Trans.* **87**, 125–128. <https://doi.org/10.1039/FT9918700125>.
42. Hori, Y., Wakebe, H., Tsukamoto, T., and Koga, O. (1995). Adsorption of CO Accompanied with Simultaneous Charge Transfer on Copper Single Crystal Electrodes Related with Electrochemical Reduction of CO₂ to Hydrocarbons. *Surf. Sci.* **335**, 258–263. [https://doi.org/10.1016/0039-6028\(95\)00441-6](https://doi.org/10.1016/0039-6028(95)00441-6).
43. Peterson, A.A., and Nørskov, J.K. (2012). Activity Descriptors for CO₂ Electroreduction to Methane on Transition-Metal Catalysts. *J. Phys. Chem. Lett.* **3**, 251–258. <https://doi.org/10.1021/jz201461p>.
44. Li, F., Thevenon, A., Rosas-Hernández, A., Wang, Z., Li, Y., Gabardo, C.M., Ozden, A., Dinh, C.T., Li, J., Wang, Y., et al. (2020). Molecular Tuning of CO₂ to Ethylene Conversion. *Nature* **577**, 509–513. <https://doi.org/10.1038/s41586-019-1782-2>.
45. Zhu, L., Lin, Y., Liu, K., Cortés, E., Li, H., Hu, J., Yamaguchi, A., Liu, X., Miyauchi, M., Fu, J., and Liu, M. (2021). Tuning the Intermediate Reaction Barriers by a CuPd Catalyst to Improve the Selectivity of CO₂ Electroreduction to C₂ products. *Chin. J. Catal.* **42**, 1500–1508. [https://doi.org/10.1016/S1872-2067\(20\)63754-8](https://doi.org/10.1016/S1872-2067(20)63754-8).
46. Wang, Q., Liu, K., Hu, K., Cai, C., Li, H., Li, H., Herran, M., Lu, Y.R., Chan, T.S., Ma, C., et al. (2022). Attenuating Metal-Substrate Conjugation in Atomically Dispersed Nickel Catalysts for Electroreduction of CO₂ to CO. *Nat. Commun.* **13**, 6082. <https://doi.org/10.1038/s41467-022-33692-0>.
47. Chang, X., Zhao, Y., and Xu, B. (2020). pH Dependence of Cu Surface Speciation in the Electrochemical CO Reduction Reaction. *ACS Catal.* **10**, 13737–13747. <https://doi.org/10.1021/acscatal.0c03108>.
48. Zheng, M., Wang, P., Zhi, X., Yang, K., Jiao, Y., Duan, J., Zheng, Y., and Qiao, S.Z. (2022). Electrocatalytic CO₂-to-C₂₊ with Ampere-level Current on Heteroatom-engineered Copper via Tuning *CO Intermediate Coverage. *J. Am. Chem. Soc.* **144**, 14936–14944. <https://doi.org/10.1021/jacs.2c06820>.
49. Iijima, G., Inomata, T., Yamaguchi, H., Ito, M., and Masuda, H. (2019). Role of a Hydroxide Layer on Cu Electrodes in Electrochemical CO₂ Reduction. *ACS Catal.* **9**, 6305–6319. <https://doi.org/10.1021/acscatal.9b00896>.
50. Shaw, S.K., Berná, A., Feliu, J.M., Nichols, R.J., Jacob, T., and Schiffrin, D.J. (2011). Role of Axially Coordinated Surface Sites for Electrochemically Controlled Carbon Monoxide Adsorption on Single Crystal Copper Electrodes. *Phys. Chem. Chem. Phys.* **13**, 5242–5251. <https://doi.org/10.1039/C0CP02064H>.
51. Wei, P., Gao, D., Liu, T., Li, H., Sang, J., Wang, C., Cai, R., Wang, G., and Bao, X. (2023). Coverage-driven Selectivity Switch from Ethylene to Acetate in High-rate CO₂/CO Electrolysis. *Nat. Nanotechnol.* **18**, 299–306. <https://doi.org/10.1038/s41565-022-01286-y>.
52. Lopez, N., and Nørskov, J. (2001). Synergistic Effects in CO Adsorption on Cu-Pd(111) Alloys. *Surf. Sci.* **477**, 59–75. [https://doi.org/10.1016/S0039-6028\(01\)00706-3](https://doi.org/10.1016/S0039-6028(01)00706-3).
53. Gajdoš, M., and Jürgen, H. (2005). CO Adsorption on Cu(111) and Cu(001) Surfaces: Improving Site Preference in DFT Calculations. *Surf. Sci.* **590**, 117–126. <https://doi.org/10.1016/j.susc.2005.04.047>.
54. Mason, S.E., Grinberg, I., and Rappe, A.M. (2004). First-principles extrapolation method for accurate CO adsorption energies on metal surfaces. *Phys. Rev. B* **69**, 161401. <https://doi.org/10.1103/PhysRevB.69.161401>.
55. Back, S., Lim, J., Kim, N.Y., Kim, Y.H., and Jung, Y. (2017). Single-Atom Catalysts for CO₂ Electroreduction with Significant Activity and Selectivity Improvements. *Chem. Sci.* **8**, 1090–1096. <https://doi.org/10.1039/C6SC03911A>.
56. Li, J., Ozden, A., Wan, M., Hu, Y., Li, F., Wang, Y., Zamani, R.R., Ren, D., Wang, Z., Xu, Y., et al. (2021). Silica-Copper Catalyst Interfaces Enable Carbon-Carbon Coupling Towards Ethylene Electrosynthesis. *Nat. Commun.* **12**, 2808. <https://doi.org/10.1038/s41467-021-23023-0>.
57. Li, J., Wang, Y., Zheng, L., Li, Y., Zhou, X., Li, J., Gu, D., Xu, E., Lu, Y., Chen, X., et al. (2019). Constraining CO Coverage on Copper Promotes High-Efficiency Ethylene Electroproduction. *Nat. Catal.* **10**, 1124–1131. <https://doi.org/10.1038/s41929-019-0380-x>.
58. Kresse, G., and Furthmüller, J. (1996). Efficiency of Ab-Initio Total Energy Calculations for Metals and Semiconductors Using a Plane-Wave Basis Set. *Comput. Mater. Sci.* **6**, 15–50. [https://doi.org/10.1016/0927-0256\(96\)00008-0](https://doi.org/10.1016/0927-0256(96)00008-0).
59. Kresse, G., and Furthmüller, J. (1996). Efficient Iterative Schemes for Ab Initio Total-Energy Calculations Using a Plane-Wave Basis Set. *Phys. Rev. B* **54**, 11169–11186. <https://doi.org/10.1103/PhysRevB.54.11169>.
60. Blöchl, P. (1994). Projector Augmented-Wave Method. *Phys. Rev. B* **50**, 17953–17979. <https://doi.org/10.1103/PhysRevB.50.17953>.
61. Kresse, G., and Joubert, D. (1999). From Ultrasoft Potentials to the Projector Augmented-Wave Method. *Phys. Rev. B* **59**, 1758–1775. <https://doi.org/10.1103/PhysRevB.59.1758>.
62. Grimme, S. (2006). Semiempirical GGA-Type Density Functional Constructed with a Long-Range Dispersion Correction. *J. Comput. Chem.* **27**, 1787–1799. <https://doi.org/10.1002/jcc.20495>.
63. Perdew, J.P., Burke, K., and Ernzerhof, M. (1996). Generalized Gradient Approximation Made Simple. *Phys. Rev. Lett.* **77**, 3865–3868. <https://doi.org/10.1103/PhysRevLett.77.3865>.
64. Mathew, K., Sundararaman, R., Letchworth-Weaver, K., Arias, T.A., and Hennig, R.G. (2014). Implicit solvation model for density-functional study of nanocrystal surfaces and reaction pathways. *J. Chem. Phys.* **140**, 084106. <https://doi.org/10.1063/1.4865107>.
65. Feng, Y., Kong, W.D., Cen, W.J., Zhou, X.Z., Zhang, W., Li, Q.T., Guo, H.Y., and Yu, J.W. (2019). Electrochemical CO₂ Reduction Reaction on M@Cu(211) Bimetallic Single-Atom Surface Alloys: Mechanism, Kinetics, and Catalyst Screening. *ACS Sustain. Chem. Eng.* **156**, 210–219. <https://doi.org/10.1021/acssuschemeng.9b05183>.
66. Ji, Y., Chen, Z., Wei, R., Yang, C., Wang, Y., Xu, J., Zhang, H., Guan, A., Chen, J., Sham, T.K., et al. (2022). Selective CO-to-acetate Electroreduction via Intermediate Adsorption Tuning on Ordered Cu-Pd Sites. *Nat. Catal.* **5**, 251–258. <https://doi.org/10.1038/s41929-022-00757-8>.
67. Zhi, X., Jiao, Y., Zheng, Y., and Qiao, S.Z. (2021). Key to C₂ Production: Selective C–C Coupling for Electrochemical CO₂ Reduction on Copper Alloy Surfaces. *Chem. Commun.* **57**, 9526–9529. <https://doi.org/10.1039/D1CC03796J>.

STAR★METHODS

KEY RESOURCES TABLE

REAGENT or RESOURCE	SOURCE	IDENTIFIER
VASP code	VASP Software GmbH	https://www.vasp.at/
VESTA software package	JP-Minerals	https://jp-minerals.org/vesta/en/
Graph plotting	Origin Lab	Origin: Data Analysis and Graphing Software (originlab.com)

RESOURCE AVAILABILITY

Lead contact

Further requests for resources should be directed to and will be fulfilled by the Lead Contact, Guoxiong Wang (wanggx@dicp.ac.cn).

Materials availability

This study did not yield new unique reagents.

Data and code availability

- The published article includes all datasets generated or analyzed during this study.
- This paper does not report original code.
- Any additional information required to reanalyze the data reported in this paper is available from the [lead contact](#) upon request.

METHOD DETAILS

The spin-polarized, periodic first-principles calculations in this work were performed using Vienna ab initio simulation package (VASP) software.^{58,59} The projector augmented wave (PAW) potentials were used for core electrons.^{60,61} We used the Perdew-Burke-Ernzerhof (PBE) functional for the DFT-D3 method for van der Waals (vdW) contributions evaluation.^{62,63} A plane-wave cut-off energy of 400 eV was used. Gamma-centralized grid of k-points of $3 \times 3 \times 1$ and $6 \times 6 \times 1$ were used for geometry optimization and electronic structural calculations. Cu lattice constant is 3.615 Å. Cu(111) model is composed of 36 Cu atoms with four layers, while Cu(100) is composed of 45 Cu atoms with five layers. The vacuum space of 15 Å was used between the slabs in z-direction. During the optimization, all of the atoms were relaxed. For M@Cu models, one of the Cu atoms on the surface was substituted by M atom. The optimization threshold was set to 10^{-6} eV and 0.02 eV/Å for electronic self-consistent loop and ionic relaxation loop. For the effect of solvent, VASPsol was used for implicit solvent model.⁶⁴ For the effect of cation, a layer of water molecules was added on the surface of catalyst and K atom was placed in the vicinity of *CO intermediate, and the convergence threshold was set to 0.05 eV/Å for saving computational cost. For the calculations of adsorption energy of intermediates (E_{ads}), E_{ads} was defined as

$$E_{\text{ads}}(M) = E_{\text{total}} - E_M - E_{\text{surface}} \quad (\text{Equation 1})$$

Where E_{total} is the calculated result of the energy of intermediate adsorbed on the surface, E_M is the energy of an isolated intermediate (M), and E_{surface} is the energy of M@Cu catalyst.

The computational hydrogen electrode (CHE) model was used to investigate the free energy profile in CO₂ electrolysis.⁷ In CHE method, the relative free energy change is calculated as

$$\Delta G = \mu[\text{product}] - \mu[\text{reactant}] - 0.5\mu\text{m}[\text{H}_2(\text{g})] + eU \quad (\text{Equation 2})$$

In this equation, μ is the chemical potential, while U is the applied electrical potential. Therefore, in the reaction step with proton-electron transfer, $\Delta G(U) = \Delta G_0(U) + neU$, where U is the potential versus the reversible hydrogen electrode, while ΔG_0 is the free energy at $U = 0$ V.

The Gibbs free energy (G) is calculated with [Equation 3](#).

$$G = E_{\text{Total}} + \text{ZPE} - TS + \int C_p dT \quad (\text{Equation 3})$$

Where E_{Total} is the total electronic energy, ZPE, S and $\int C_p dT$ are the zero-point vibrational energy, entropy and heat capacity at 298.15 K and 1 atm, respectively.

For evaluation of stability of M@Cu, the dissolution potentials (U_{dis} , in V) at pH = 0 was used.⁶⁵

$$U_{dis} = U_M^0 + [E_{M,bulk} - (E_{M@Cu} - E_{Cu})] / ne \quad (\text{Equation 4})$$

Where U_M^0 is the standard dissolution potential of M in bulk form. $E_{M,bulk}$ is the energy of one M atom in the bulk. $E_{M@Cu}$ and E_{Cu} are the total energy of M@Cu, and Cu with one M atom being removed, respectively. n is the coefficient in the M dissolution reaction: $M + nH^+ \rightarrow M^{n+} + n/2H_2$.

The binding energy of M (E_B , in eV) was calculated using:

$$E_B = E_{M@Cu} - E_{Cu} - E_{M,bulk} \quad (\text{Equation 5})$$

Where $E_{M@Cu}$ and E_{Cu} are the total energy of M@Cu, and Cu with one M atom being removed, respectively. $E_{M,bulk}$ is the energy of one M atom obtained from DFT energies of the bulk metal.

In the generation of C_2 products the energy barrier for the formation of *COCO from two *CO species can reflect the reactivity, facilitating a straightforward comparison of catalytic activity differences between catalysts.^{16,66} Researchers proposed that the energy for *COCO shows a good linear relationship with the activation energy for *CO coupling.⁵⁷ Therefore, the formation energy of *COCO intermediate can conveniently and accurately assess differences in catalyst activity. We used the formation energy of *COCO as the indicator for activity toward C_2 production.